Citation for published version:
Bull, S, Chiereghin, N, Gursul, I & Cleaver, D 2018, 'Unsteady Aerodynamics of a Transient Plunging Airfoil' Paper presented at AIAA Scitech 2018, Kissimmee, USA United States, 8/01/18 - 12/01/18, pp. 1-25.
https://doi.org/10.2514/6.2018-0353

DOI:
10.2514/6.2018-0353

Publication date:
2018

Document Version
Peer reviewed version

Unsteady Aerodynamics of a Transient Plunging Airfoil

S. C. Bull[1], N. Chiereghin[2], I. Gursul[3] and D. J. Cleaver[4]
University of Bath, Bath, England BA2 7AY, United Kingdom

In this study lift, pitching moment and particle image velocimetry (PIV) measurements are presented for a NACA 0012 airfoil with a Reynolds number of 20,000 at a geometric angle of attack in the range 0° to 20° undergoing a transient plunging motion. The transient motion is defined by a Strouhal number based on the chord length up to 0.60 and effective plunge angle amplitude from -30° to 30°. The largest peak in both lift and pitching moment was observed during the motion for all cases. This was attributed primarily to circulatory effects for the lift and added-mass effects for pitching moment. PIV showed the presence of a coherent leading-edge vortex (LEV) at positive plunge angle amplitudes which had the biggest effect on the pitching moment during motion. Substantial peaks in lift and pitching moment were observed for post-stall geometric angles of attack after the end of motion. This is postulated to be due to strong interactions between the leading and trailing-edge vortices. An increase in plunge angle amplitude caused an increase in the magnitudes of lift/moment change. This shedding phenomena was found for both positive and negative plunge angles and showed remarkably similar peak relative timings, highlighting the insensitivity of the shedding process to the initial transient forcing.

Nomenclature

α_0 = geometric angle of attack
α_{eff} = effective angle of attack, $\alpha_0 + \tan^{-1}(U_{pl}/U_\infty)$
α_{pl} = effective angle of attack induced by motion, $\tan^{-1}(U_{pl}/U_\infty)$
$\alpha_{pl,max}$ = amplitude of effective angle of attack induced by motion
b = wing spanwise length
c = chord
C_L = static lift coefficient, $L/0.5\rho U_\infty^2 cb$
ΔC_L = lift coefficient relative to C_L
$\Delta C_{L,P1}$ = magnitude of 1st peak in relative lift coefficient
$\Delta C_{L,P2}$ = magnitude of 2nd peak in relative lift coefficient
$\Delta C_{L,P3}$ = magnitude of 3rd peak in relative lift coefficient
$C_{M,1/4}$ = static quarter-chord pitching moment coefficient, $M_{1/4}/0.5\rho U_\infty^2 c^2 b$
$\Delta C_{M,1/4}$ = quarter-chord pitching moment coefficient relative to $C_{M,1/4}$
$\Delta C_{M,1/4,P1}$ = magnitude of 1st peak in quarter-chord pitching moment coefficient
$\Delta C_{M,1/4,P2}$ = magnitude of 2nd peak in quarter-chord pitching moment coefficient
$\Delta C_{M,1/4,P3}$ = magnitude of 3rd peak in quarter-chord pitching moment coefficient
f = frequency, $1/T$
L = lift force
Re = Reynolds number,
Sr_c = Strouhal number based on chord, fc/U_∞
t = time

---

[1] PhD Researcher, Department of Mechanical Engineering.
[2] Research Associate, Department of Mechanical Engineering, Member AIAA.
[3] Professor, Department of Mechanical Engineering, Associate Fellow AIAA.
[4] Lecturer, Department of Mechanical Engineering, Member AIAA.

T = motion period, $2\Delta T_p + \Delta T_h$
ΔT_p = duration of ramp to and from $\alpha_{pl,max}$
ΔT_h = duration of hold at $\alpha_{pl,max}$, 0.05τ
τ = convective time, tU_∞/c
U_{pl} = plunge velocity
U_∞ = freestream velocity

I. Introduction

PLUNGING airfoils and wings have been a subject of interest across a range of applications. In the low Reynolds number regime, studies have used plunging airfoils to represent the wing kinematics of biological flyers so as to understand the mechanisms for high lift and efficient thrust generation [1–3]. In recent years, the focus has shifted to the potential of micro air vehicles (MAVs) to exploit these unsteady mechanisms in order to overcome problems associated with low Reynolds number flight [4–7]. In the high Reynolds number regime, research has focused towards the problems of flutter [8] and helicopter rotor blade flapping [9, 10]. Recent studies have also used plunging airfoils to represent vertical gust disturbances [11, 12]. Despite the lack of direct equivalence between a plunging airfoil and vertical gust, Wong *et al.* [11] highlight the benefits of this approach, namely the repeatability of the gust profile.

A common feature in all these scenarios is the presence of coherent leading edge vortices (LEVs), which can form due to flow separation during unsteady motion. These LEVs can substantially increase both time-averaged [7] and peak lift [12], produce large excursions in nose-down pitching moment and introduce significant non-linearity to the aerodynamic loads [6, 9, 13]. Predicting such loads are important in the design of both low Reynolds number MAVs and high Reynolds number civil aircraft. For civil aircraft extreme gusts encounters can determine the limits of structural design and be detrimental to passenger comfort. Current methods of prediction are either inaccurate in these highly separated vortical flows or entail an infeasible computational cost. As a result, civil aircraft designers must apply large safety factors to the estimated gust loads to account for this uncertainty, leading to over-sized structures. An early step in addressing this problem is to further understand the effect of unsteady vortical flows on aerodynamic loads. Experimental testing over large parameter sweeps can shed light on underlying trends, validate computational fluid dynamics (CFD) methods and inform the development of reduced-order models.

A large proportion of plunging airfoil studies have used periodic motions, typically sinusoidal, when simplifying the unsteady problem. This is a valid approach for naturally periodic scenarios such as flapping flight or helicopter rotor blades, however for transient scenarios such as manoeuvres and discrete gusts, non-periodic motions are a closer representation [14]. There has been a recent focus on experimental transient motion studies in pitching, surging and rotating [14–18] wings and efforts to model them [19–21], as they present a richer problem for MAV applications. Notable transient plunging motion studies include a ramp-hold [22, 23] and a ramp-hold-return [14] plunge velocity function, although they are quite limited in scope. These studies have documented the formation of a strong LEV that leads to large overshoots in lift, not unlike similar periodic cases. The added-mass effect, due to the acceleration of the local fluid, becomes significant at higher reduced frequencies, which also depends on the transient motion profile. Transients have been shown to either converge to a steady-state condition in around four convective times after the motion has ended [14, 22] or show significant undulations long after motion cessation [15, 18, 22, 23]. This appears to be dependent on the angle of attack of the airfoil at the end of motion, with post-stall angles displaying longer transients.

In the present paper, the ramp-hold-return function from Ol *et al.* [14] shown in Fig. 1 is tested across a range of Strouhal numbers and effective angles of attack that cover the gust range for civil aircraft [24]. Corresponding lift and pitching moment data is presented along with phase-averaged PIV measurements of the velocity field for select cases. The aim is to directly measure lift and pitching moment during transient motions, to highlight salient features and explain the underlying flow physics.

II. Experimental Method

The experiment consists of a NACA 0012 airfoil with a geometric angle of attack, α_0, plunging normal to the free stream velocity, as shown in Figure 1a. The plunge velocity, U_{pl}, creates an effective angle of attack, α_{pl}, which varies during the motion. Figure 1b shows the generalized transient motion profile, taken from Ol *et al.* [14], whereby the effective angle of attack, α_{pl}, is increased linearly for the duration, ΔT_p, held constant at a maximum, $\alpha_{pl,max}$, for the interval ΔT_h and linearly returned to zero for the duration ΔT_p. The Strouhal number based on chord, Sr_c, is defined by the motion period, T, which can be varied by altering the ramp duration, ΔT_p, whilst the holding the duration of hold constant at 0.05τ [14]. Unlike Ol *et al.* [14], no smoothing was applied to the ramp-hold-return function as this profile describes the velocity rather than the position of the plunging airfoil. After motion cessation, the airfoil was held static for 30 convective time units, τ, to allow the flow to achieve steady-state conditions. Phase-averaged lift and pitching moment were obtained across Sr_c=0.05 to 0.60, with $\alpha_{pl,max}$ up to -30 and +30°, depending on a displacement constraint. With this test matrix, four geometric angles of attack, α_0, were selected to represent pre-stall (0°), stall (9°) and post-stall (15°, 20°) regimes.

A. Experimental Facility

The experiments were conducted in the water tunnel facility at the University of Bath. This has a close-loop free surface configuration with a glass working section of dimensions 381 x 508 x 1530 mm. The tunnel is capable of a free stream velocity of up to 0.5 m/s and has a reported turbulence intensity of less than 0.5% [25]. The plunging motion is supplied by a stepper motor driven Zaber LSQ150B-T3 linear stage with an X-MCB1 controller that connects to a carriage mounted on shafts that run through four frictionless air bushings. Such a setup constrains the assembly to axial motion only within a positional accuracy of 5%. Quasi-2D conditions were achieved through the use of an upper and lower splitter plate with a 1 mm clearance at the root and tip, shown in Figure 2. The quasi-2D assumption of this set up in static conditions has been verified by Chiereghin *et al.* [12] through bending moment measurements that show the center of lift located at the mid-span. The wing consists of a NACA 0012 profile with a chord length c=62.7 mm and an aspect ratio of AR=5. This was manufactured using selective laser sintering (SLS), finished with a polished smooth-at-touch surface and painted matt black for PIV measurements. To provide spanwise stiffness, a T800 carbon fiber insert was slotted along the span at the quarter chord location. The wing is mounted vertically to the rig through a rotation stage that gives angle of attack changes with an accuracy of ±0.2°.

B. Load measurements

A Futek S-beam tension/compression load cell acts as the link between the motion stage and the carriage in order to measure the force normal to the free stream, see Figure 2. The frictionless air bushings constrain the motion to a single degree of freedom and enable precise measurement of the axial force. For the pitching moment measurements, a Futek reaction torque sensor was mounted between the wing and the carriage with the reference axis located at the quarter-chord location, see Figure 2. The data acquisition system (DAQ) was set to 2000 samples per period. Each case was repeated 30 times and then averaged. For static measurements, the data was acquired for 40 seconds at a sample rate of 1kHz. With this set up, the raw load cell and torque sensor signals will contain both aerodynamic and inertial mass components. In order to isolate the aerodynamic component, an accelerometer was mounted to the moving section of the rig. The acceleration signal was then multiplied by the moving mass and subtracted from the raw load cell and torque sensor signals. The moving mass for each sensor was determined by applying a sinusoidal motion to the rig in air and dividing the first harmonic of each load sensor by the first harmonic of the accelerometer signal. Once the signals were phase-averaged, a 3rd order Butterworth band stop filter was applied remove the dominant wing and rig vibration frequencies and a moving average filter was applied at 50Hz.

C. Particle Image Velocimetry

2D particle image velocimetry (PIV) images were taken at cross-sectional spanwise plane located at the mid-span of the wing as shown in Figure 2a. The laser was located to the side of the working section which illuminates the airfoil upper surface with a Nd:YAG 50 mJ pulsed laser sheet. The water was seeded with commercially available hollow glass particles of 8-12 μm in nominal diameter. To capture the images, a 4 mega pixel CCD camera was positioned below at a slight offset to eliminate shadow from the wing tip on the suction surface. The image pairs were analyzed in TSI's software package Insight 4G™ using a fast Fourier transform correlator on an interrogation window size of 32 x 32 pixels with a window displacement of 25%, giving a special resolution of approximately 0.8mm (1.3% of the chord length). Erroneous vectors were replaced with the local median in the post-processing stage. Flow field measurements were conducted during and after the motion, triggered through a Renishaw optical linear encoder and TSI synchronizer. For each measurement point, 100 image pairs were obtained and averaged.

III. Results

Part A presents lift and pitching moment time-histories to highlight common features across the test matrix. Part B investigates the fluid dynamic cause of these features through PIV measurements for four example cases. In Part C, the time-histories are reduced to the magnitude and phase of the peaks present in the time-histories to determine the sensitivity of these features.

A. Lift and Pitching Moment Measurements

Figure 3 presents the static measurements for the lift and quarter-chord pitching moment coefficient from -20 to +20°. In Figure 3a, the static lift coefficient shows excellent agreement with measurements previously conducted at the University of Bath by Chiereghin *et al.* [12], using the current lift measurement system, and Cleaver *et al.* [26], who measured lift via a binocular strain gauge force balance. A significant degree of non-linearity can be seen in the lift curve slope. A plateau is observed at low angles of attack, 0 to +2°, before increasing significantly in gradient from 2 to 4° and is in line with previous low Reynolds number studies [27, 28], see Figure 3a. Kim *et al.* [27] attributed this region of non-linearity to laminar separation of the boundary layer from 0 to 2° followed by an abrupt reattachment at 3°, corresponding to the significant increase in lift curve slope. The lift curve then shows a decreasing gradient up to 9° before exhibiting an abrupt stall. Wang *et al*. [28] showed the formation of a laminar separation bubble in this region which introduces non-linearity. Good agreement can be observed between the measured lift and literature [27–29] for low angles of attack, however the stall region shows significant discrepancies. The static lift curve at low Reynolds numbers, $O(10^4)$, is highly sensitive to both turbulence intensity [28] and Reynolds number [28, 29]. In Figure 3b the static pitching moment coefficient measurements are compared with Ohtake *et al*. [30] and show good agreement for a similar Reynolds number. It is currently unclear as to the cause of the undulations seen in Figure 3b, however they are most likely related to the laminar boundary layer behavior at these low Reynolds numbers.

Figure 4 presents the time-histories for ΔC_L and $\Delta C_{M,1/4}$ at $Sr_c=0.45$ and $\alpha_{pl,max}=\pm25°$ across the range of geometric angles of attack, α_0. The start and end of motion are indicated by vertical dotted lines and the motion end is defined as $\tau=0$. This is a typical case, the main features are generally consistent across the Sr_c range but become more pronounced with increasing $\alpha_{pl,max}$. This will be shown later in Part C. Cases with a positive $\alpha_{pl,max}$ will be referred to as positive motion whereas cases with a negative $\alpha_{pl,max}$ will be referred to as negative motion.

Figure 4a shows the variation in ΔC_L during positive motion at $\alpha_{pl,max}=+25°$. At the start of the motion ΔC_L exhibits a steep gradient before increasing almost linearly, with a slight bump halfway through, to a maximum around mid-motion. A short plateau in the lift response can be observed, followed by an initial rapid decline before exhibiting a more gradual decrease to motion cessation. During the motion all α_0 display the same behavior. Perhaps the most interesting feature of this is section is that there is little difference in the lift response during motion across the α_0 range. It was shown by Chiereghin *et al* [12] that the flow around a NACA0012 airfoil at $\alpha_0=0°$ will experience separation onset at an effective angle of attack of 25°. For stall and post-stall angles of attack however, a coherent LEV is formed which leads to a significantly increased time-averaged lift coefficient. A similar effect would be expected here due to the similarities in forcing conditions yet the responses remain remarkably similar. The main difference appears as a slight variation in the maximum ΔC_L during the motion, with $\alpha_0=9$, 15° exhibiting slightly larger maximum ΔC_L peak than $\alpha_0=0$, 20°, however these differences are close to the uncertainty of the lift measurement.

In the post-motion stage, $\tau>0$, the response of ΔC_L shows distinct changes with α_0, see Figure 4a. For both $\alpha_0=0$, 9° the lift decays gradually to steady-state at approximately $\tau=6$. Interestingly $\alpha_0=9°$ shows lower lift in this region. For the post-stall cases, $\alpha_0=15$ and 20°, the lift response shows significant undulations taking up to 10-12 convective times to approach the steady-state value. At $\alpha_0=15°$ the lift response displays an increase in lift around $\tau=4$ followed by a gradual decrease approaching steady state around $\tau=10$. At $\alpha_0=20°$ the post-motion lift response displays multiple maxima, which is indicative of large scale vortex shedding [15, 18, 31]. The first post-motion peak is much larger than for $\alpha_0=15°$ and occurs about 1τ prior. The subsequent peak occurs around $\tau=6$ after a delay of approximately 3.5τ. The convective time delay between the two post-motion peaks is in line with transient studies by Mulenners *et al.* [18] and Rosti *et al.* [23] who show a similar time delay of $3.7\text{-}4.0\tau$ between vortex shedding peaks.

Figure 4b shows the $\Delta C_{M,1/4}$ response for the same cases as Figure 4a. As α_0 is increased, the magnitude of nose-down pitching moment during the ramp-up stage increases whilst the peak in nose-up pitching moment during the ramp-down stage is progressively decreased. Shortly after motion cessation, the pitching moment displays another nose-down peak at around $\tau=0.5\text{-}1$. It will be shown later that this is due to the formation and shedding of a coherent LEV. Figure 4b also highlights the vortex shedding behavior at a post-stall α_0 with the post-motion peak locations roughly coinciding with the corresponding ΔC_L peaks in Figure 4a.

Figure 4c and Figure 4d presents ΔC_L and $\Delta C_{M,1/4}$ at Sr_c=0.45 for the negative motion, $\alpha_{pl,max}$=-25°. Considering first the lift response in Figure 4c, a similar behavior can be seen across the range of α_0. A sharp drop in lift is seen followed by a linear decrease to a minimum at around t/T=0.5. The lift then sharply increases before exhibiting a more gradual increase to motion cessation. A noteworthy feature for these cases is the absent of the nose-down pitching peak shortly after the end of motion as there is no upper surface LEV forming and shedding for the negative cases during motion. Similar to the positive motion cases, there is then a difference between α_0=0, 9° and post-stall α_0=15, 20°. For α_0=0, 9° the lift shows a similar gradual decay approaching steady-state at τ=6. The post-stall cases however show a surprising similarity to the positive cases. A single increase in lift before a gradual decay to steady-state can be seen for α_0=15° whilst α_0=20° displays the vortex shedding behavior with similar peak locations.

B. Flow Field Measurements

To elucidate the underlying flow structures behind the features presented in Figure 4, flow field measurements are presented for positive cases with Sr_c=0.45, $\alpha_{pl,max}$=+25° and α_0=9,15 and 20° as well as a negative case for Sr_c=0.45, $\alpha_{pl,max}$=-25° and α_0=15°. Alongside the flow fields the corresponding time-histories of lift force and pitching moment are also presented. On these time-histories the various peaks are highlighted and labelled with their time of occurrence for cross-reference with the PIV time stamps. An estimation of the added-mass force component is also plotted for lift and pitching moment. This estimate was based on the well-established Theodorsen model [32], who proposed the added-mass force is proportional to the product of the plunging acceleration, measured using an accelerometer, and the mass of a local fluid column of diameter c.

Figure 5 presents the stall case of α_0=9°. Figure 5a presents the change in lift coefficient as a function of non-dimensional time, τ, relative to the static case, Figure 5b presents the change in pitching moment coefficient, and Figure 5c the vorticity flow field at various values of τ. The flow fields are arranged in a column format with clockwise/positive vorticity shown in red and counter clock-wise/negative vorticity shown in blue.

For this case the motion starts at τ=-2.2. During the initial acceleration, τ=-2.2 to -2.0, it is clear that the initial lift and pitching moment increase is dominated by the added-mass component, shown in Figure 5a and 5b. As the effective angle of attack increases, τ =-1.7 to -1.4, the upper surface shear layer begins to roll up into small coherent structures. At this point a maximum nose-down pitching moment is observed, see Figure 5b. By τ=-1.1 a strong coherent leading-edge vortex has formed whilst the small structures from the initial shear layer are shed into the wake. At this point in the motion the airfoil is producing the maximum ΔC_L. The relative lift time-history shows that the circulatory lift is most dominant component in the maximum ΔC_L during motion, with the added-mass contributing a relatively small amount. Once the maximum ΔC_L has been reached the lift drops rapidly due to the sign change in added-mass and decreasing α_{pl}. At τ=-0.5 the LEV has reached its maximum size. A region of secondary counter-clockwise vorticity between the vortex and airfoil is generated which intersects and cuts off the feeding shear layer prior to the shedding process [33]. At this time instant the circulatory force is directly counteracted by the large negative added-mass component resulting in a change in lift coefficient near to zero. The impact of the LEV is also apparent in the pitching moment measurements. The added-mass prediction shows an approximately constant value of $\Delta C_{M,1/4}\approx$-0.4 during the acceleration phase; followed by an approximately constant value of $\Delta C_{M,1/4}\approx$0.4 during the deceleration phase. During the acceleration phase, τ=-2.2 to -1.1, the measured moment demonstrates similar trends to the added-mass. However, during the deceleration phase, τ=-1.1 to 0, there is a significant difference, with the experiment consistently exhibiting a lower pitching moment. Once the motion is complete, τ= 0, the experimental measurement demonstrates a large nose-down $\Delta C_{M,1/4}$. This consistently lower pitching moment correlates with the inception of the LEV at $\tau\approx$-1.7, growth $-1.7<\tau<-0.5$, detachment and convection, $-0.5<\tau$. As the LEV convects over the upper surface, it moves further from the quarter-chord point producing a larger nose-down $\Delta C_{M,1/4}$ which can be seen in Figure 5b. When the LEV moves over the trailing edge it triggers the formation of a trailing-edge vortex (TEV) which coincides with the distinct nose-down $\Delta C_{M,1/4}$ peak [13] between 0.0-1.0τ. The LEV/TEV pair then shed into the free-stream as the well documented "mushroom" shape dipole [6, 34] visible at τ=1.0. Past this point the vorticity indicates some separation on the upper surface, but with little effect on the lift/pitching moment which approaches steady-state by around τ=6.0.

Figure 6 presents the same Sr_c and $\alpha_{pl,max}$ but with α_0 increased to 15°. Before the motion starts at τ=-2.2 the flow is in a fully separated state, indicated by the separated shear layers from the leading and trailing edge. From τ=-2.2 to τ=-2.0 the added-mass force is the dominant component in the lift increase which is reinforced by the unchanged separated state of the flow. By τ=-1.4 the leading and trailing edge shear layers have started to roll up into distinct vortices and the shear layer aft of the vortices begins to shed into the wake. The point of maximum ΔC_L once again occurs at τ=-1.1 where there is a strong LEV at the leading edge. A striking difference between this case and α_0=9° is the LEV position which is further above the upper surface and further downstream. As the motion progresses the gap between the vortex and the upper surface increases considerably compared with α_0=9° and the feeding shear layer is dragged upwards. Due to the increased distance between the vortex and the upper surface there is less secondary vorticity generated at the airfoil surface. Despite this the feeding shear layer is still cut off at τ=-0.5. The LEV then convects across the upper surface at an increased velocity compared with Figure 5. This is possibly in part due to a lower self-induced velocity of the LEV with a greater distance from the airfoil surface [35]. By τ=0.0 the LEV has reached the trailing edge and promotes the formation of a new TEV. A lower peak nose-down pitching moment is observed compared with α_0=9° at τ=0.5. The passage of the LEV at a greater vertical distance induces a weaker TEV which in turn produces a lower suction peak at the trailing edge. By τ=1.0 the LEV has been completely shed and the TEV is fully formed. At this point the lift and nose-down pitching moment begin to steadily increase over the next 3 convective times resulting in a maximum at around τ=4. The flow field measurements indicate that the influence of the induced TEV deflects the leading edge shear layer towards the airfoil surface and promotes roll up into a secondary leading edge vortex, albeit much less coherent. This can be seen to cover the entire airfoil upper surface at τ=4.0, corresponding to the point of peak loads. This diffuse vortex passes over the trailing edge at τ=5.0 inducing a much weaker tertiary TEV, although this has no effect on the aerodynamic loads.

Figure 7 shows the same forcing parameters as Figure 5 and Figure 6 but with the angle increased again to α_0=20°. The vorticity distribution for the first portion of the motion is very similar to that of α_0=15°. The differences start to become apparent at τ=-1.4 where the LEV starts to lift off the surface. A stronger nose-down pitching moment is produced here, see Figure 7b, far exceeding the added-mass contribution. At τ=-1.1 the LEV is a significant distance from the upper surface, indicating the LEV vertical position is a function of α_0. Despite the increased distance from the surface, the maximum ΔC_L is similar to α_0=9° and 15°. In the latter portion of the motion the LEV is marginally higher above the airfoil surface than α_0=15°, see Figure 6c and Figure 7c. The LEV can also be seen to be further along the airfoil chord, indicating an increase in convection speed. As the LEV passes the trailing-edge a strong nose-down pitching moment peak occurs in Figure 7b around τ=0.5. The LEV triggers the formation of a secondary TEV which is slightly stronger compared with α_0=15°. The roll up of the leading edge shear layer occurs sooner at τ=3.0, corresponding to the peak in both lift and nose-down pitching moment. At τ=3.0 the vorticity distribution shows a stronger, more coherent vortical structure over the upper surface of the airfoil, giving rise to a larger peak in lift and nose-down pitching moment. A tertiary TEV is then formed as the secondary LEV passes over the trailing-edge, which in turn influences the leading-edge shear layer, promoting further roll up. A weaker third peak in lift and nose-down pitching moment can be seen in Figure 7 at $\tau\approx$6.5, corresponding to the formation of the tertiary LEV that has formed over the upper surface. This vortex shedding process is damped out at around 12 convective times where the lift and pitching moment approach steady-state.

It is then evident from the flow field measurements at α_0=20° that the periodic fluctuations in lift are caused by periodic vortex shedding. From comparing the flow fields for α_0=15° and α_0=20° it can be seen that the post-motion increase in lift is caused by the same mechanism, yet α_0=15° only displays a single shedding cycle whereas α_0=20° shows two shedding cycles. Through comparison with studies by Mulenners *et al.* [18] and Rosti *et al.* [23] it can be seen that remarkably similar vortex shedding phenomena can occur for different transient motions, such as plunge and surge. The post-motion peaks caused by vortex shedding all occur around 3.5-4.0 convective times apart and show a decay in amplitude as the process is damped out. In the study by Mulenners *et al.* [18] a surging flat plate at α_0=30° exhibited three additional peaks after the passage of the primary LEV, indicating a decay rate dependency on the geometric angle of attack and airfoil geometry. The computational study by Rosti *et al.* [23] however showed that a NACA0020 profile will produce several peaks with a low decay rate at α_0=20°. This decrease in peak decay rate is most likely due to the spanwise periodic boundary conditions applied to the simulation leading to stronger, more coherent structures, as shown by Visbal and Garmann [36], throughout the shedding process which are able to induce stronger subsequent vortices.

A negative motion case equivalent to Figure 6 is presented in Figure 8 to elucidate the mechanism for the post motion peaks. During the acceleration phase the leading edge shear layer is pushed back onto the airfoil surface resulting in attached flow. The reattachment point propagates downstream towards the trailing edge at roughly the free-stream velocity from τ=-1.7 to τ=-0.5. At this point a small trailing edge vortex has formed due to the proximity of the deflected leading-edge shear layer. At motion cessation, the flow is fully attached and the lift response starts to increase almost linearly as the influence of the TEV diminishes through convection into the wake. During this time positive vorticity begins to accumulate on the upper surface and roll up into small coherent structures, as seen at τ=1.0. At τ=2.0 these are shed into the wake, as indicated by a small roll up in the trailing edge shear layer, and upper surface vorticity begins to accumulate just aft of the leading edge. During τ=2.0 to τ=3.0 this region of vorticity propagates downstream and begins to lift off forming a vortex over the upper surface. This bears strong resemblance to τ=4.0 for the positive case in Figure 6 and produces a similar magnitude peak in both lift and pitching moment. A TEV vortex is induced as the LEV passes the trailing edge from τ=5.0 to τ=6.0 but, like the positive case, has no discernable impact on the loads.

C. Peak Loads

The main features in the lift and pitching moment response have been highlighted as a first peak during the motion followed by potentially multiple post-motion peaks. The initial peak during the motion is primarily due to circulation increase due to the effective angle of attack; the post-motion peaks observed for post-stall α_0 are associated with large-scale vortex shedding initiated by the motion. This section will reduce the time-histories across the entire test matrix to extract their main features enabling comparison across a wide parameter range.

Figure 9 presents the maximum relative lift and pitching moment coefficients during motion, denoted P1, plotted against Sr_c for each $\alpha_{pl,max}$ across the α_0 range. Values of small Sr_c and high $\alpha_{pl,max}$ could not be tested due to the displacement amplitude constraint, i.e., proximity of the water tunnel walls. Consider first the distribution of $\Delta C_{L,P1}$ in Figure 9 for each geometric angle of attack. The lift at P1 is relatively insensitive to Sr_c at every α_0 for both positive and negative motions and shows a monotonic increase with $\alpha_{pl,max}$. Figure 10 plots this data against $\alpha_{pl,max}$ and demonstrates a monotonic relationship across the test matrix. An insight into the insensitivity of $\Delta C_{L,P1}$ to Sr_c can be gained by considering the total lift force as the sum of its circulatory and added-mass components. In section B it was shown that the more dominant component of the lift at P1 was circulatory through comparison of the total lift response with the estimated added-mass contribution. This was only marginally affected by separation and the onset of LEV formation as shown by the similar lift response across α_0 during the motion. As a result, the lift variation up to P1 can be considered as a buildup of circulation with the added-mass force superposed [19, 37].

The negative motion shows more variation with α_0. At α_0=0° the distribution is a mirror image of the positive motion as expected by symmetry. As the geometric angle of attack is increased the magnitude of $\Delta C_{L,P1}$ decreases quite considerably, particularly for higher $\alpha_{pl,max}$ values at post-stall α_0 values. This is likely due to the influence of the separated flow on the upper surface of the airfoil at post-stall angles of attack, an example of which is shown in Figure 8.

In terms of pitching moment, Figure 9 shows a distinct difference between geometric angles of attack. Note here that the negative values of $\Delta C_{M,1/4,P1}$ relate to the positive motion. For α_0=0°, the magnitude of $\Delta C_{M,1/4,P1}$ for both positive and negative motion shows a monotonic increase with $\alpha_{pl,max}$. As α_0 is increased to stall and post-stall angles the negative motion peaks follow a similar monotonic trend, whilst the positive motion peak magnitudes show an increased magnitude with $\alpha_{pl,max}$. From Figure 6 and Figure 7 it can be seen that this coincides with the formation of the initial TEV which acts at a large moment arm from the quarter-chord axis. In contrast to the lift at P1, the pitching moment does not collapse as well with Sr_c, see Figure 10, possibly due to the large influence of the added-mass.

Figure 11 presents the timings of P1 in terms of the normalized time t/T. The results show that overall for a higher Sr_c, the lift and moment peaks occur earlier in the motion, from around τ=-0.5 to τ=-0.7. This remains valid across all geometric angles of attack and shows virtually no variation with $\alpha_{pl,max}$. The reasons for the slight variation in P1 with Sr_c is not currently clear.

The magnitude of the first post-motion peak loads, P2, for the post-stall angles of attack are shown in Figure 12. Considering first $\Delta C_{L,P2}$ for the positive motion at α_0=15°. The peak magnitudes show a linear increase with $\alpha_{pl,max}$, indicating a dependency on the strength of the initial LEV formed during the motion which triggers the shedding process. Interestingly a higher Sr_c produces a larger peak lift at lower $\alpha_{pl,max}$ values whilst the opposite is true at higher $\alpha_{pl,max}$ values. The cause of this behavior is elucidated by Eslam Panah and Buchholz [35] who demonstrated a lower LEV circulation at higher frequency plunging oscillations for the same effective angle of attack (equivalent to $\alpha_{pl,max}$ here) due to the gestation time for full LEV development. The maximum $\Delta C_{L,P2}$ reached for positive motion cases are $\Delta C_{L,P2}$=1.1 for α_0=15° and $\Delta C_{L,P2}$=1.5 for α_0=20°. A similar trend in $\Delta C_{L,P2}$ is seen for α_0=20°. The gradient of $\Delta C_{L,P2}$ with $\alpha_{pl,max}$ shows a dependency on α_0, with α_0=20° displaying a higher gradient. The same Sr_c based behavior of the peak strengths is also seen for this case. For the negative motion cases, $\Delta C_{L,P2}$ asymptotically approaches a relatively lower maximum lift with $\alpha_{pl,max}$ than the positive motion, $\Delta C_{L,P2}$=0.8 for α_0=15° and $\Delta C_{L,P2}$=1.2 for α_0=20°, and shows little change with Sr_c. The point of saturation for $\Delta C_{L,P2}$ occurs at a higher $\alpha_{pl,max}$ for α_0=20°.

The timings of P2 for the lift and pitching moment are shown in Figure 13 and are presented in terms of convective times after motion cessation. For positive and negative motion at both α_0, the times of P2 are on average later for an increased Sr_c and show more variation at lower values of $\alpha_{pl,max}$. Consider first the positive motion. From the discussion in the previous section, P2 was shown to occur once the initial LEV had passed the trailing edge, triggering a secondary TEV. As a first approximation to this, the convection speed of the LEV can be assumed constant. A higher Sr_c would therefore mean the LEV would be at a greater distance from the trailing edge at τ=0.0, taking a longer time to reach the trailing edge and trigger the secondary TEV. This behavior is more or less reflected in Figure 13. Deviation from this trend occurs at higher $\alpha_{pl,max}$ magnitudes. For α_0=15° the higher Sr_c produces an earlier peak in lift and pitching moment for positive motion. The cause of this is unclear at this time, but could be due to the influence of initial LEV strength on the vortex convection speed [35]. For the negative motion this Sr_c dependency is most likely due to finite response time of the flow. For a higher Sr_c, the circulation will have had less time to respond to the changing effective angle of attack and so the flow would take a relatively longer time to develop into a post-motion LEV as seen in Figure 8. The peak locations for negative motion also tend to converge at high $\alpha_{pl,max}$ values. For α_0=20° the peak locations for lift and pitching moment display the same relation with Sr_c and $\alpha_{pl,max}$ with the peaks occurring approximately one convective time prior to that of α_0=15°. The influence of α_0 on the timing of $\Delta C_{L,P2}$ has been shown in Figure 7 to be due to an earlier roll up of the leading-edge shear layer and is interesting to see occurring across the whole parameter range.

It can be seen in Figure 13 that more scatter is present in the data for lift peak location than for the pitching moment. This suggests smoother pitching moment peaks that are less affected by vorticity fluctuation which would be a more reliable visualization for peak timing trends, as they have been shown to coincide with the lift peaks through the same flow mechanism.

Figure 14 presents the peak magnitudes for the second post-motion peak, P3, for the lift and pitching moment coefficient for α_0=20°. It is important to note that some low frequency, low amplitude cases have been omitted from the results as they did not produce a discernable peak after P2. Manar *et al.* [31] postulate that this is likely due to a lack of vortex circulation strength necessary for strong vortex shedding. As seen from the previous section the magnitudes are lower than for P2 which corresponds to the decay in vortex coherency during each shedding cycle, see Figure 7. Mulleners *et al.* [18] attribute this decay to movement of the interaction location between the LEV and TEV, however there is insufficient temporal resolution in the PIV images to corroborate this. Interestingly both the lift and pitching moment display the same trends as P2 for α_0=15, 20°. The magnitude of $\Delta C_{L,P3}$ increases almost linearly with $\alpha_{pl,max}$ for the positive motion, albeit at a lower gradient than seen in Figure 12. The same Sr_c based behavior of the peak strengths is also shown. For the negative motion Sr_c has almost no effect and the peak magnitudes saturate at an $\alpha_{pl,max}$=20°. The similarities of the peak magnitude trends for P2 and P3 highlight the dependence of P3 on P2. A stronger vortex over the upper surface of the airfoil at P2 will induce a stronger vortex shedding cycle.

The timings of P3 are shown in Figure 15. More data points were omitted due to the increased sensitivity of the peak detection criteria for particularly low peaks with a shallow gradient. Despite this, comparisons can still be made for the timings of P2 in Figure 13. A similar trend for timings of P3 can be seen. The convective times between the peaks P2 and P3 is around 3-3.5τ across the test matrix, which is in line with previous studies [18, 23] and highlights the dominance of the convective time scale on the vortex shedding frequency rather than the initial transients.

In summary, the peak during the motion (P1) is driven primarily by circulatory and added-mass effects for the lift and pitching moment respectively; whereas the post-motion peaks (P2 and P3) are caused by large scale vortex shedding where the maximum load corresponds to the formation of a secondary/tertiary vortex over the upper surface of the airfoil. This was observed for post-stall angles of attack only. The magnitude of P2 showed a strong dependence on the maximum plunge angle whilst P3 showed a similar trend to P2 with a reduced magnitude. A similar time delay of 3-3.5τ between P2 and P3 could be seen across the test matrix, showing the relative insensitivity of the vortex shedding frequency to the forcing conditions.

IV. Conclusions

Transient plunging motion of a NACA 0012 airfoil was investigated across a large parameter range to give an insight into the underlying trends of the vortical behavior that can occur at high effective angles of attack. The peak lift during motion was found to be primarily due a buildup of the circulatory component. Conversely the peak pitching moment magnitude was found to be primarily dependent on the added-mass force. At stall and post-stall angles of attack a coherent LEV is formed over the upper surface of the airfoil for positive effective plunge angles. For post-stall angles of attack significant undulations in the post-motion load time-histories were observed. Flow field measurements revealed this to be caused by large scale vortex shedding, in which the shedding of a leading-edge vortex (LEV) triggers the formation of a trailing-edge vortex (TEV) which in turn triggers the formation of a new LEV. This process is repeated until there is sufficient decay where no new vortex is formed. An increase in effective angle of attack amplitude showed an increase in peak lift/moment magnitudes. The vortex shedding phenomena was found for both a positive and negative excursion in effective angle of attack and showed remarkably similar peak relative timings, highlighting the insensitivity of the process to the initial transient forcing.

Acknowledgments

This research is sponsored by Engineering and Physical Sciences Research Council (EPSRC) through grant numbers EP/M022307/1, EP/K040391/1 and EP/M000559/1. The authors acknowledge Ashutosh Pardesi for his help in the data acquisition.

q

References

[1] Freymuth, P., “Three-Dimensional Vortex Systems of Finite Wings,” *Journal of Aircraft*, Vol. 25, 1988, pp. 971–972.

[2] Triantafyllou, M. S., Triantafyllou, G. S., and Gopalkrishnan, R., “Wake mechanics for thrust generation in oscillating foils,” *Physics of Fluids A: Fluid Dynamics*, Vol. 3, 1991, pp. 2835–2837.

[3] Anderson, J. M., Streitlien, K., Barrett, D. S., and Triantafyllou, M. S., “Oscillating foils of high propulsive efficiency,” *Journal of Fluid Mechanics*, Vol. 360, 1998, pp. 41–72.

[4] Tuncer, I. H., and Platzer, M. F., “Computational Study of Flapping Airfoil Aerodynamics,” *Journal of Aircraft*, Vol. 37, 2000, pp. 514–520.

[5] Young, J., and Lai, J. C. S., “Mechanisms Influencing the Efficiency of Oscillating Airfoil Propulsion,” *AIAA Journal*, Vol. 45, 2007, pp. 1695–1702.

[6] Rival, D., and Tropea, C., “Characteristics of Pitching and Plunging Airfoils Under Dynamic-Stall Conditions,” *Journal of Aircraft*, Vol. 47, 2010, pp. 80–86.

[7] Cleaver, D. J., Wang, Z., Gursul, I., and Visbal, M. R., “Lift Enhancement by Means of Small-Amplitude Airfoil Oscillations at Low Reynolds Numbers,” *AIAA Journal*, Vol. 49, 2011, pp. 2018–2033.

[8] Halfman, R. L., *Experimental Aerodynamic Derivatives of a Sinusoidally Oscillating Air-foil in Two-Dimensional Flow*, NACA-TR-1108, 1952.

[9] Carta, F. O., *A Comparison of the Pitching and Plunging Response of an Oscillating Airfoil*, NASA-CR-3172, 1979.

[10] Maresca, C. A., Favier, D. J., and Rebont, J. M., “Unsteady Aerodynamics of an Aerofoil at High Angle of Incidence Performing Various Linear Oscillations In A Uniform Stream,” *Journal of the American Helicopter Society*, Vol. 26, 1981, pp. 40–45.

[11] Wong, J. G., Mohebbian, A., Kriegseis, J., and Rival, D. E., “Rapid flow separation for transient inflow conditions versus accelerating bodies: An investigation into their equivalency,” *Journal of Fluids and Structures*, Vol. 40, 2013, pp. 257–268.

[12] Chiereghin, N., Cleaver, D., and Gursul, I., “Unsteady Measurements for a Periodically Plunging Airfoil,” *55th AIAA Aerospace Sciences Meeting*, Grapevine, TX, AIAA Paper, 2017-0996, 2017.

[13] Visbal, M. R., “Numerical Investigation of Deep Dynamic Stall of a Plunging Airfoil,” *AIAA Journal*, Vol. 49, 2011, pp. 2152–2170.

[14] Ol, M. V., Eldredge, J. D., and Wang, C., “High-Amplitude Pitch of a Flat Plate: an Abstraction of Perching and Flapping,” *International Journal of Micro Air Vehicles*, Vol. 1, 2009, pp. 203–216.

[15] Ol, M. V., and Babinsky, H., “Unsteady Flat Plates: a Cursory Review (Invited),” *54th AIAA Aerospace Sciences Meeting*, San Diego, CA, AIAA Paper, 2016-0285, 2016.

[16] Jones, A. R., Manar, F., Phillips, N., Nakata, T., Bomphrey, R., Ringuette, M. J., Percin, M., van Oudheusden, B., and Palmer, J., “Leading Edge Vortex Evolution and Lift Production on Rotating Wings (Invited),” *54th AIAA Aerospace Sciences Meeting*, CA, AIAA Paper, 2016-0288, 2016.

[17] Son, O., Cetiner, O., Stevens, P. R. R. J., Babinsky, H., Manar, F., Mancini, P., Jones, A. R., Ol, M. V., Gozukara, A. C., Number, R., Engineer, S. A., and Engineer, S., “Parametric Variations in Aspect Ratio , Leading Edge and Planform Shapes for the Rectilinear Pitch Cases of AVT-202,” *American Institute of Aeronautics and Astronautics*, CA, AIAA Paper, 2016-0289, 2016.

[18] Mulleners, K., Mancini, P., and Jones, A. R., “Flow Develpment on a Flat-Plate Wing Subjected to a Stremwise Acceleration,” *AIAA Journal*, Vol. 55, 2017, pp. 2118-2122.

[19] Pitt Ford, C. W., and Babinsky, H., “Lift and the leading-edge vortex,” *Journal of Fluid Mechanics*, Vol. 720, 2013, pp. 280–313.

[20] Babinsky, H., and Stevens, P. R. R. J., “Low Order Modelling of Lift Forces for Unsteady Pitching and Surging Wings,” *54th AIAA Aerospace Sciences Meeting*, CA, AIAA Paper, 2016-0290, 2016.

[21] Ramesh, K., Gopalarathnam, A., Edwards, J. R., Ol, M. V., and Granlund, K., “An unsteady airfoil theory applied to pitching motions validated against experiment and computation,” *Theoretical and Computational Fluid Dynamics*, Vol. 27, 2013, pp. 843–864.

[22] Pitt Ford, C. W., and Babinsky, H., “Impulsively Started Flat Plate Flow,” *AIAA Journal*, Vol. 46, 2009, pp. 1800–1802.

[23] Rosti, M. E., Omidyeganeh, M., and Pinelli, A., “Direct numerical simulation of the flow around an aerofoil in ramp-up motion,” *Physics of Fluids*, Vol. 28, 2016.

[24] European Aviation Safety Agency, *Certification Specifications for Large Aeroplanes CS-25*, 2007.

[25] Heathcote, S. F., “Flexible Flapping Airfoil Propulsion at Low Reynolds Numbers,” Ph.D. Dissertation,

Department of Mechanical Engineering, Univ. of Bath, Bath, England, U.K., 2006.

[26] Cleaver, D. J., Wang, Z., and Gursul, I., “Vortex Mode Bifurcation and Lift Force of a Plunging Airfoil at Low Reynolds Numbers,” *48th AIAA Aerospace Sciences Meeting*, Orlando, FL, AIAA Paper, 2010-390, 2010.

[27] Kim, D. H., Chang, J.-W., and Chung, J., “Low-Reynolds-Number Effect on Aerodynamic Characteristics of a NACA 0012 Airfoil,” *Journal of Aircraft*, Vol. 48, 2011, pp. 1212–1215.

[28] Wang, S., Zhou, Y., Alam, M., Yang, H., Wang, S., Zhou, Y., Alam, M., and Yang, H., “Turbulent intensity and Reynolds number effects on an airfoil at low Reynolds numbers,” *Physics of Fluids*, Vol. 26, 2014.

[29] Schluter, J. U., “Lift Enhancement at Low Reynolds Numbers Using Self-Activated Movable Flaps,” *Journal of Aircraft*, Vol. 47, 2010, pp. 348–351.

[30] Ohtake, T., Nakae, Y., and Motohashi, T., “Nonlinearity of the aerodynamic characteristics of NACA 0012 aerofoil at low Reynolds number,” *The Japan Society for Aeronautical and Space Science*, Vol. 55, 2007, pp. 439–445.

[31] Manar, F., Mancini, P., Mayo, D., and Jones, A. R., “Comparison of Rotating and Translating Wings: Force Production and Vortex Characteristics,” *AIAA Journal*, Vol. 54, 2015, pp. 519–530.

[32] Theodorsen, T., “General theory of aerodynamic instability and the mechanism of flutter,” *NACA-TR-496*, 1935.

[33] Rival, D., Kriegseis, J., and Schaub, P., “A criterion for vortex separation on unsteady aerodynamic profiles,” *51st AIAA Aerospace Sciences Meeting*, Grapevine, TX, AIAA Paper, 2013-0836, 2013.

[34] Panda, J., and Zaman, K. B. M. Q., “Experimental investigation of the flow field of an oscillating airfoil and estimation of lift from wake surveys,” *Journal of Fluid Mechanics*, Vol. 265, 1994, pp. 65–95.

[35] Eslam Panah, A., and Buchholz, J. H. J., “Parameter dependence of vortex interactions on a two-dimensional plunging plate,” *Experiments in Fluids*, Vol. 55, 2014, p. 1687.

[36] Visbal, M. R., and Garmann, D. J., “Numerical Investigation of Spanwise End Effects on Dynamic Stall of a Pitching NACA 0012 Wing,” *55th AIAA Aerospace Sciences Meeting*, Grapevine, TX, 2017-1481, 2017.

[37] Wong, J. G., Kriegseis, J., and Rival, D. E., “An investigation into vortex growth and stabilization for two-dimensional plunging and flapping plates with varying sweep,” *Journal of Fluids and Structures*, Vol. 43, 2013, pp. 231–243.

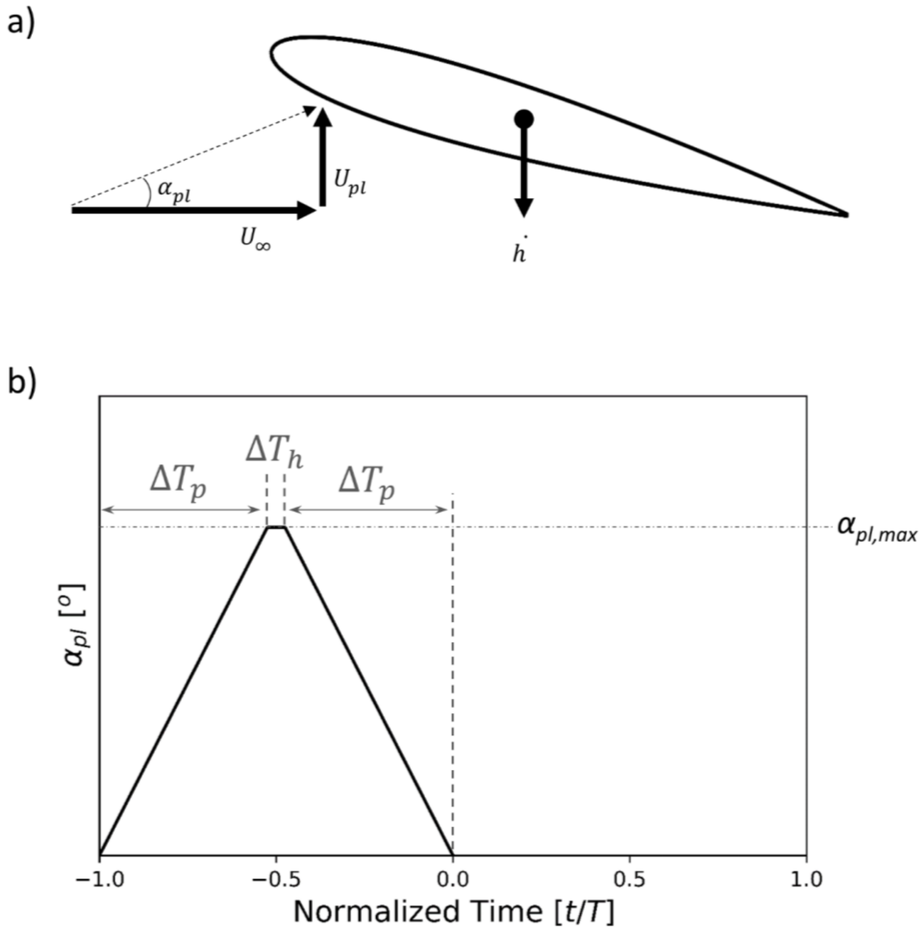

Figure 1. a) Airfoil plunging motion parameters; b) profile of effective angle of attack for transient plunging motion

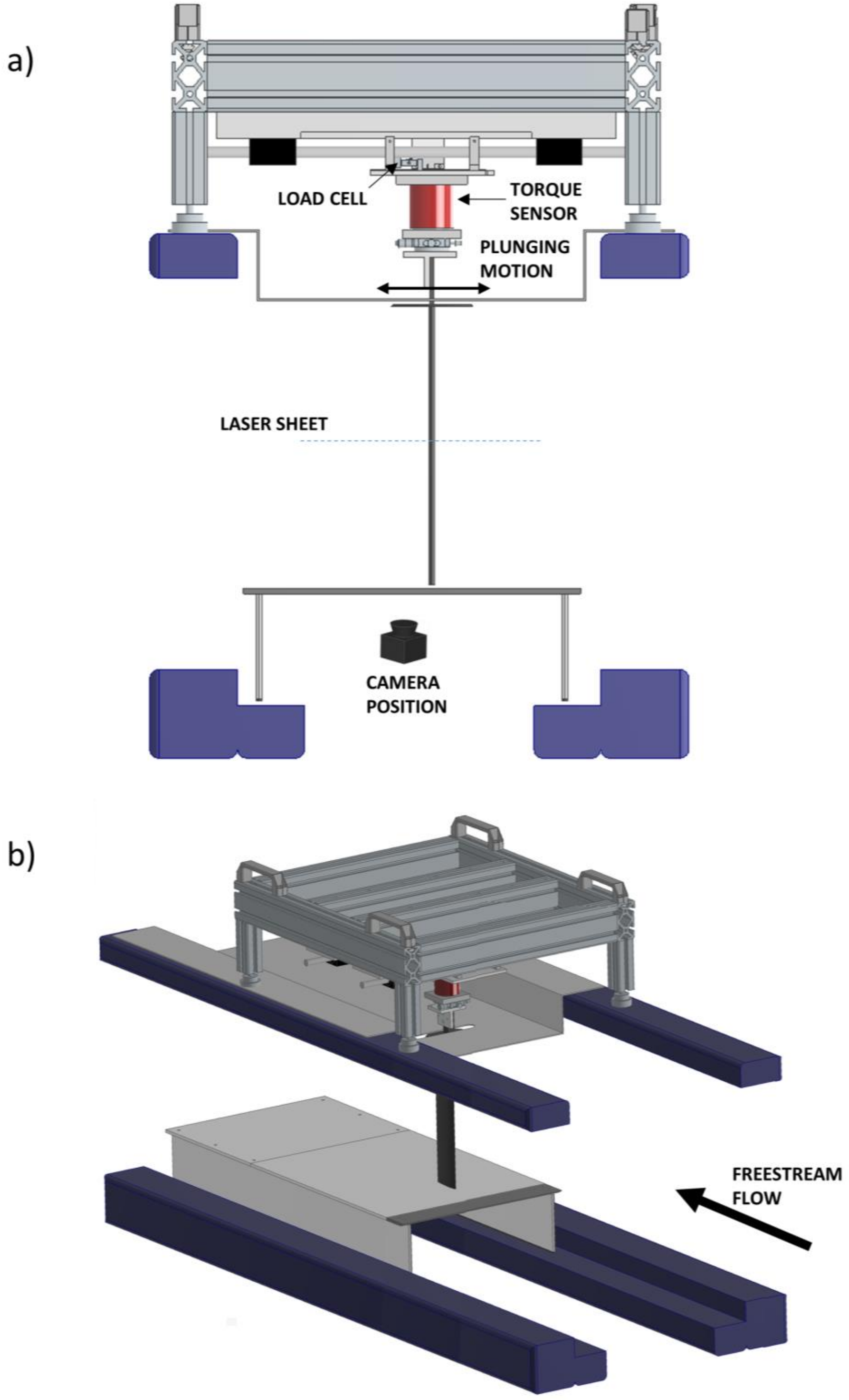

Figure 2. Test rig a) front view b) isometric view

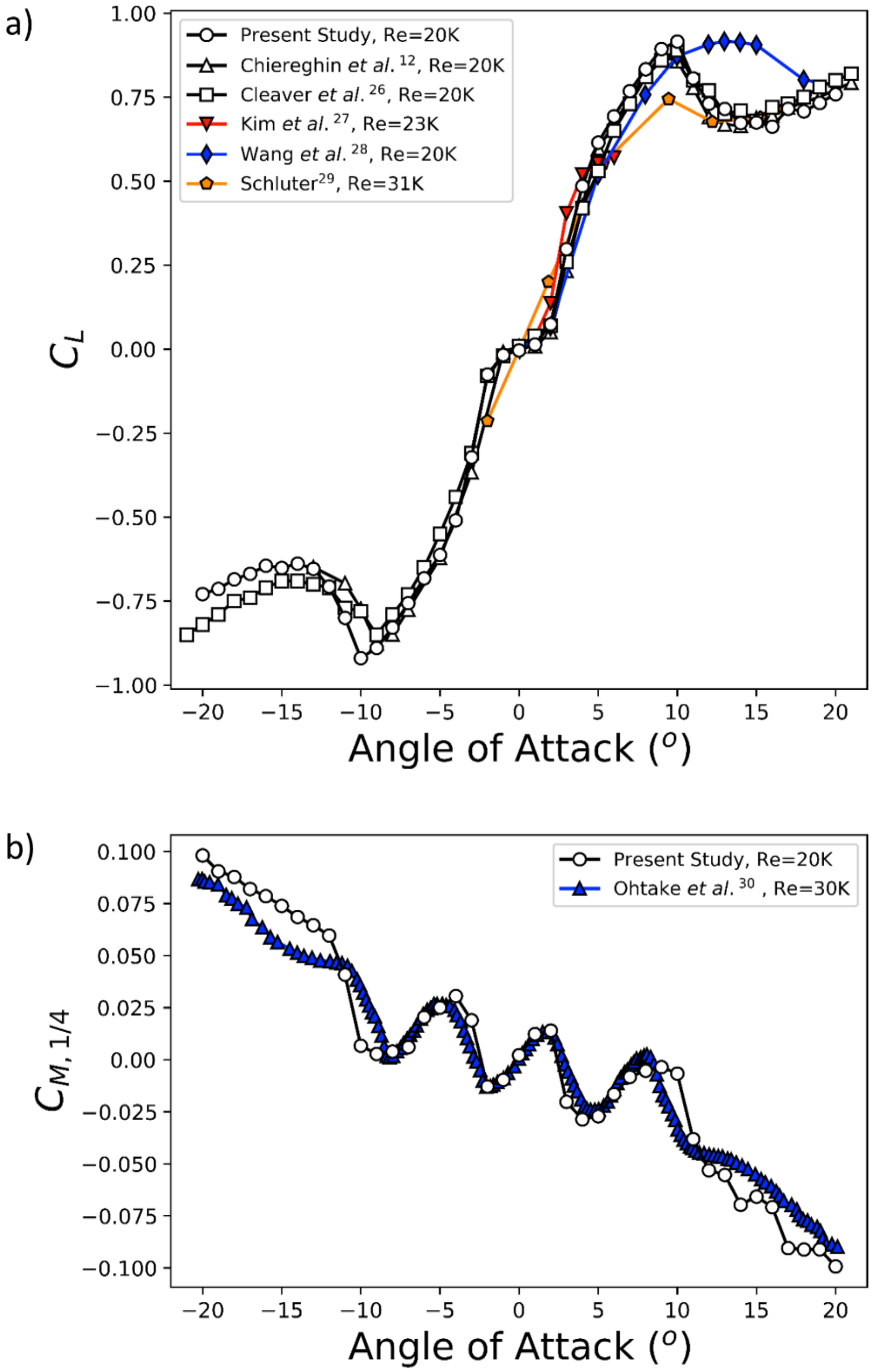

Figure 3. Static measurements of; a) lift coefficient, C_L; b) pitching moment coefficient about the quarter chord, $C_{M,1/4}$.

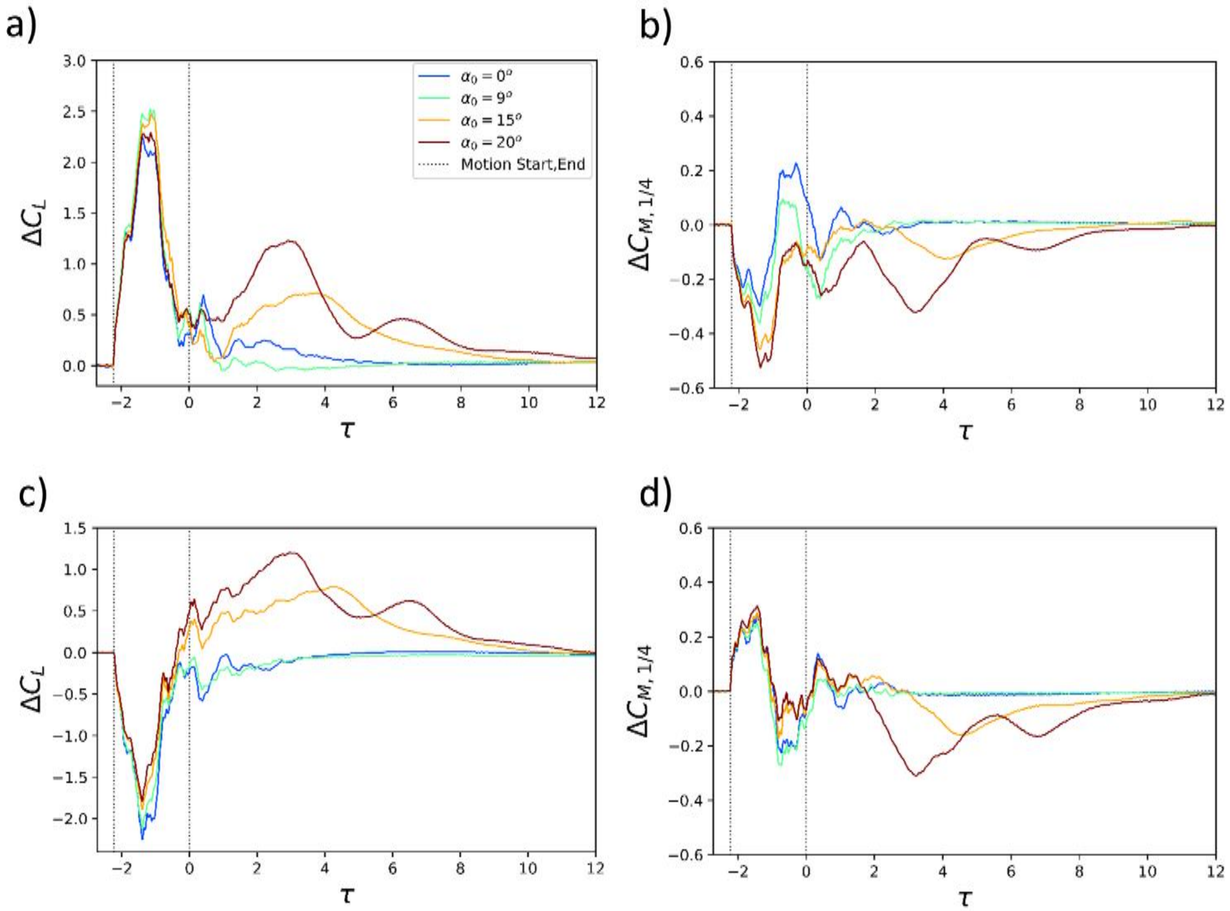

Figure 4: Relative lift and moment coefficient time-histories across the geometric angle of attack range for Sr_c=0.45: a) ΔC_L for $\alpha_{pl,max}$ =+25º (positive motion); b) $\Delta C_{M,1/4}$ for $\alpha_{pl,max}$ =+25º (positive motion); c) ΔC_L for $\alpha_{pl,max}$=-25º (negative motion); d) $\Delta C_{M,1/4}$ for $\alpha_{pl,max}$=-25º (negative motion).

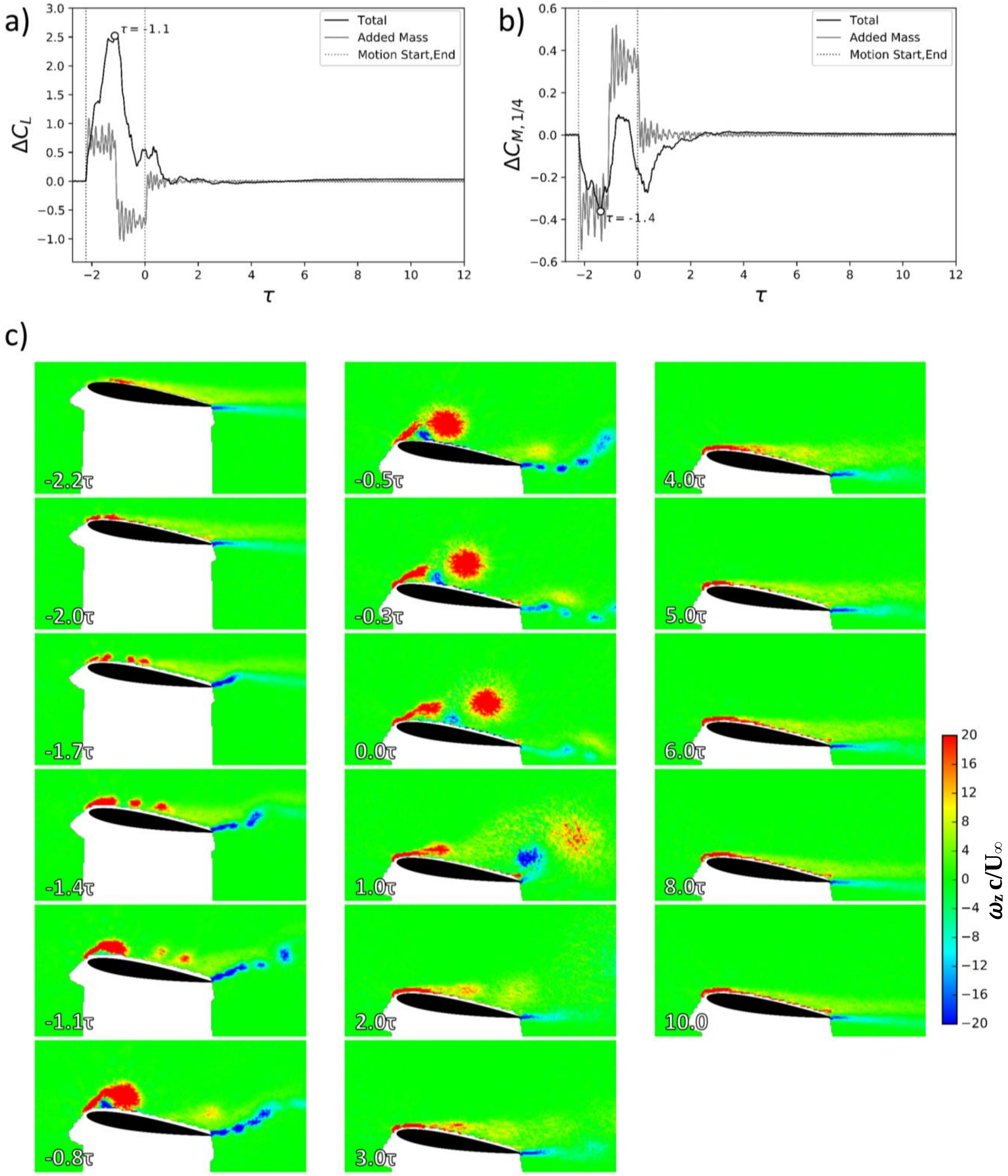

Figure 5. α_0**=9º for** Sr_c**=0.45,** $\alpha_{pl,max}$**=+25º: a) relative lift and b) relative pitching moment time-history with added-mass estimation, and c) phase-averaged normalized spanwise vorticity at selected times.**

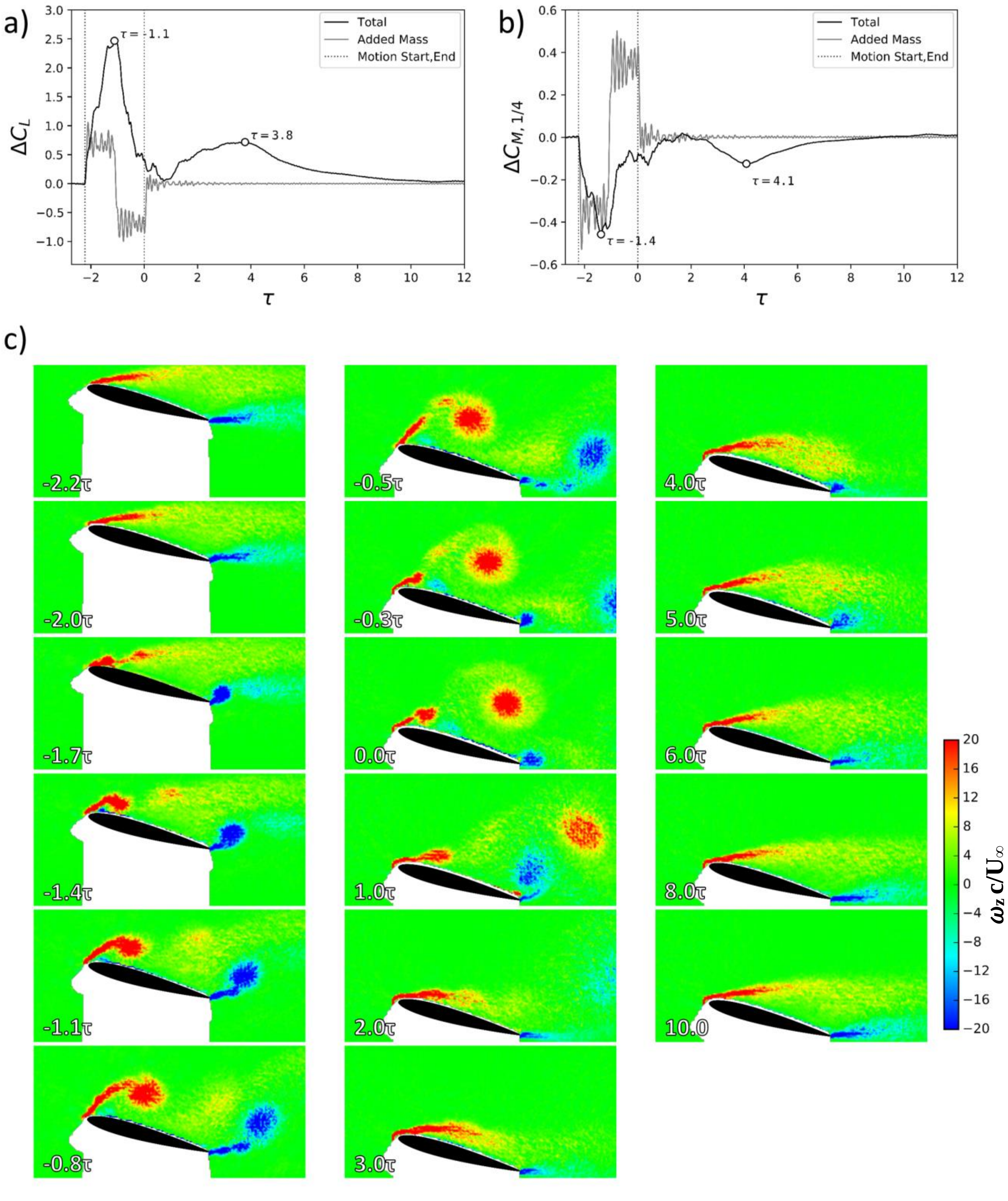

Figure 6. α_0**=15º for** Sr_c**=0.45,** $\alpha_{pl,max}$**=+25º: a) relative lift and b) relative pitching moment time-history with added-mass estimation, and c) phase-averaged normalized spanwise vorticity at selected times.**

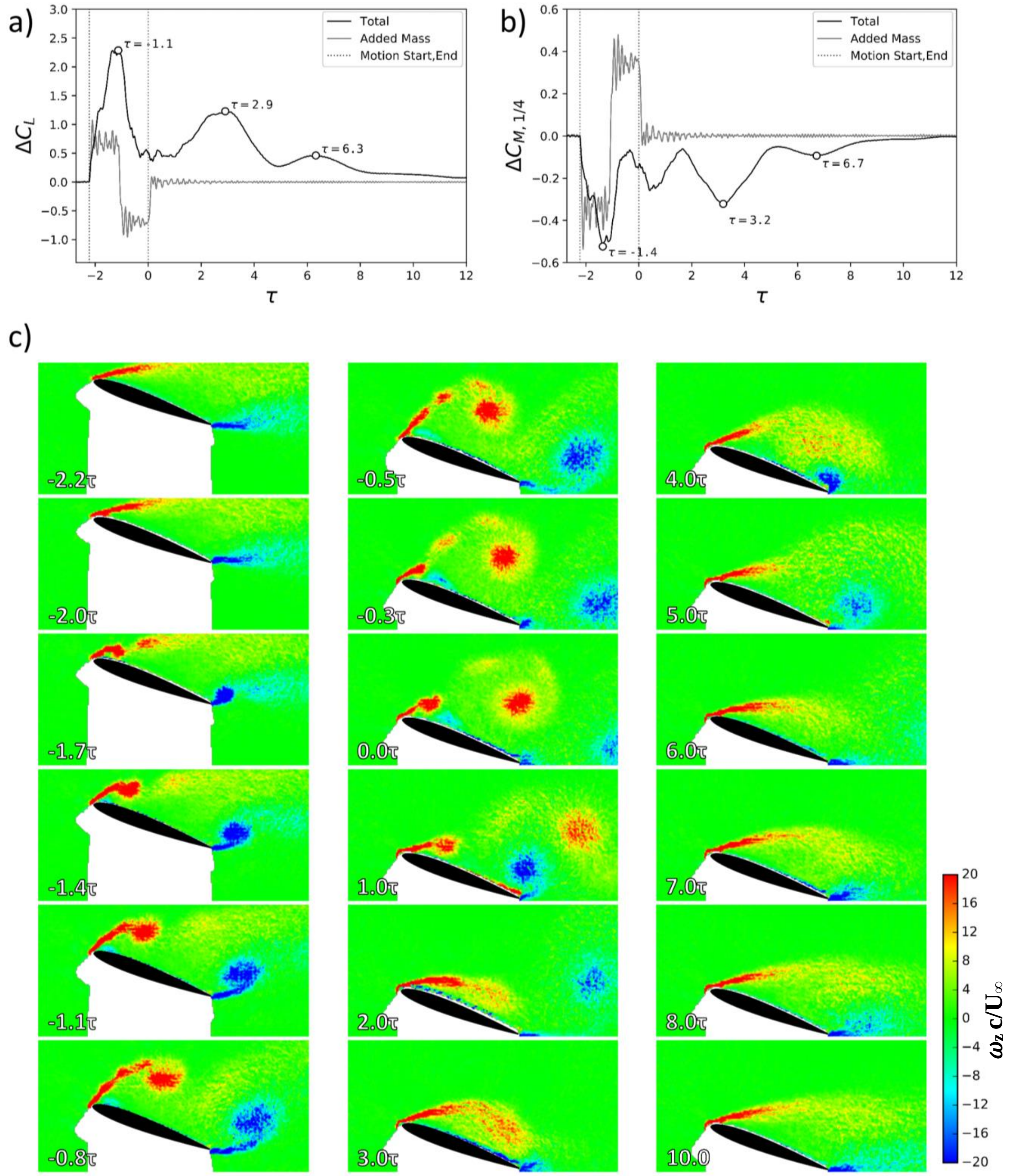

Figure 7. α_0=20^o for Sr_c=0.45, $\alpha_{pl,max}$=+25^o: a) relative lift and b) relative pitching moment time-history with added-mass estimation, and c) phase-averaged normalized spanwise vorticity at selected times

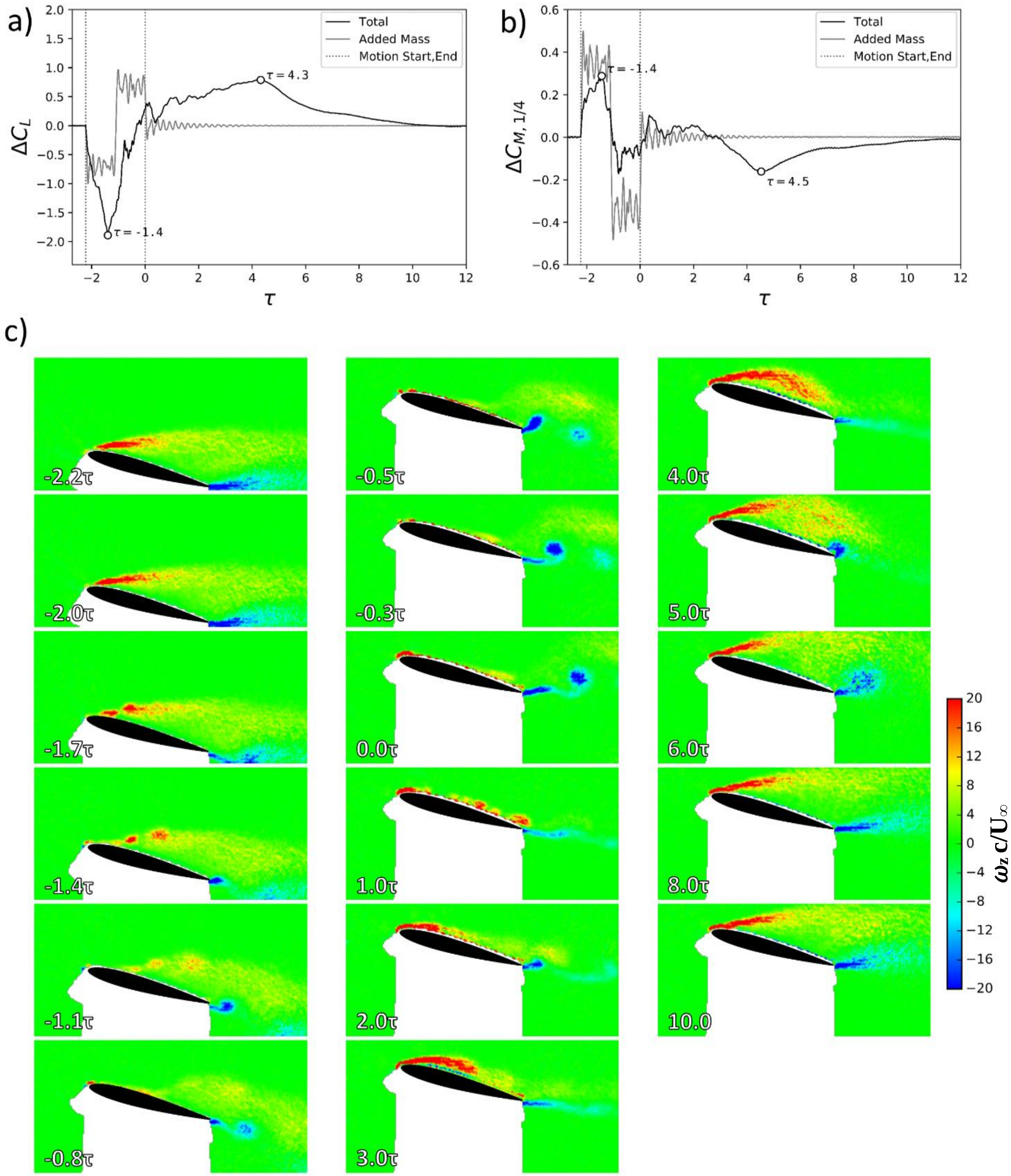

Figure 8. α_0**=15º for** Sr_c**=0.45,** $\alpha_{pl,max}$**=-25º: a) relative lift and b) relative pitching moment time-history with added-mass estimation, and c) phase-averaged normalized spanwise vorticity at selected times.**

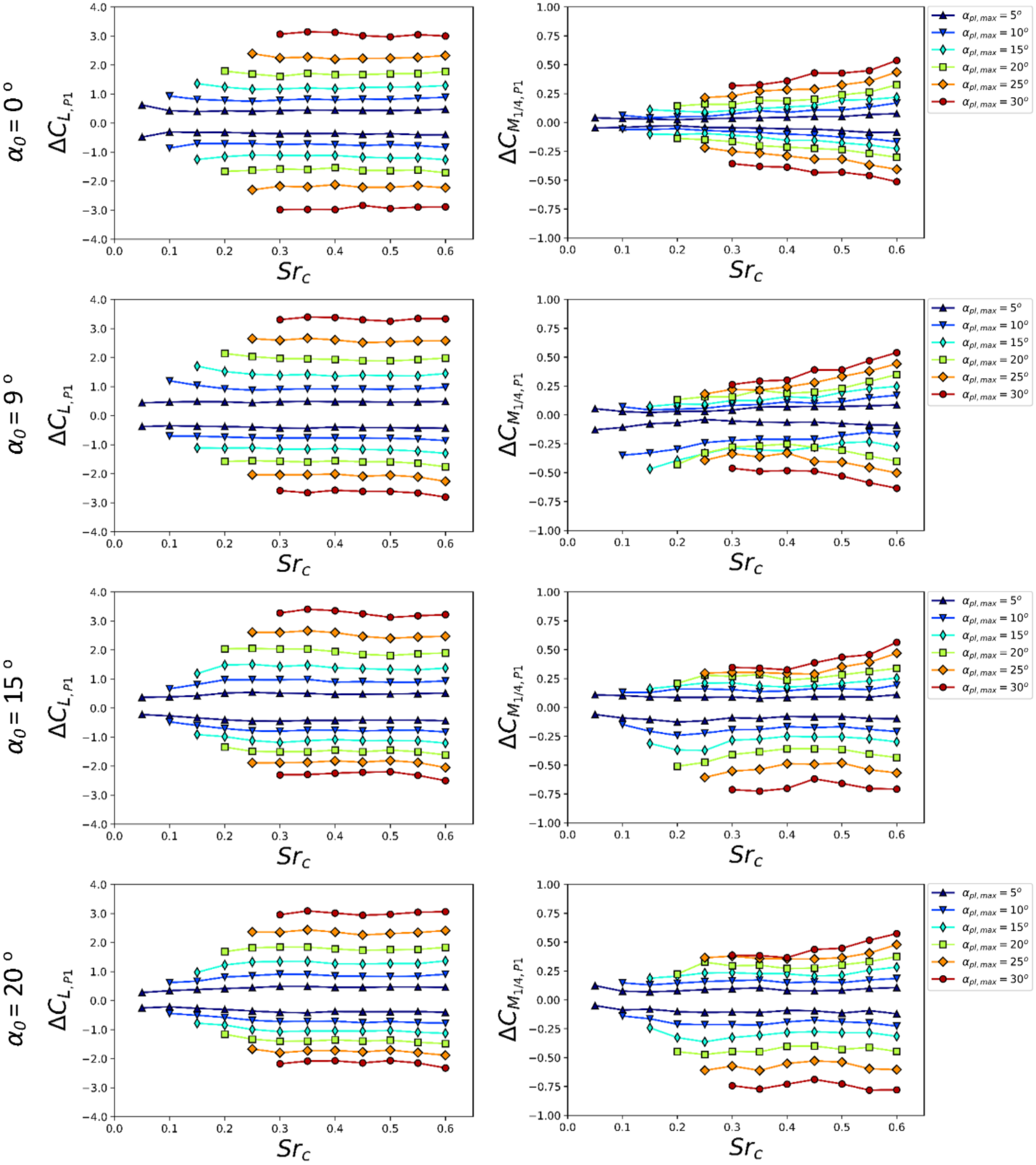

Figure 9. 1st peak relative lift coefficient, $\Delta C_{L,P1}$, and pitching moment coefficient, $\Delta C_{M,1/4,P1}$, with Sr_c for different $\alpha_{pl,max}$ across the range of α_0.

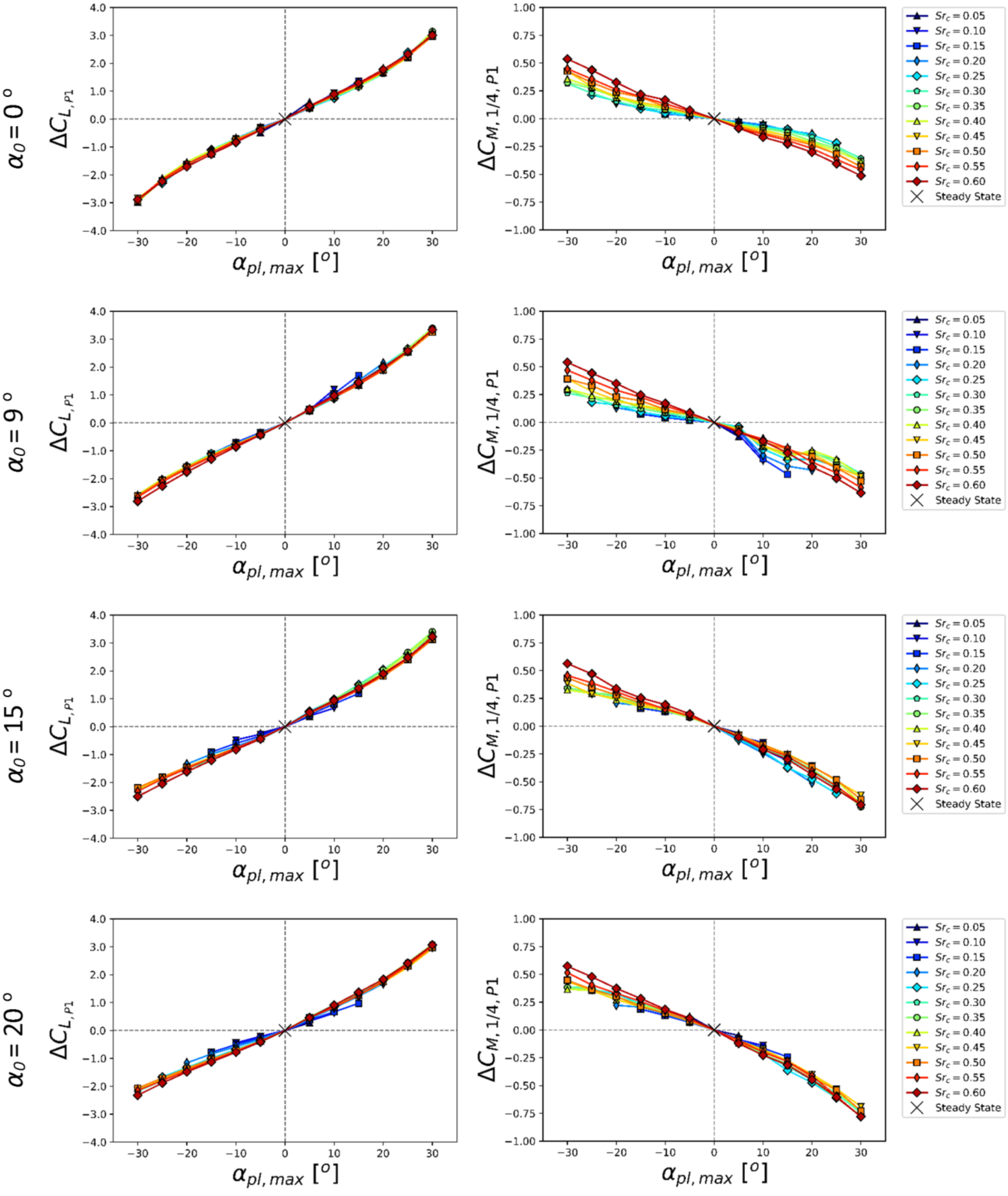

Figure 10. 1st peak relative lift coefficient, $\Delta C_{L,P1}$, and pitching moment coefficient, $\Delta C_{M,1/4,P1}$, with $\alpha_{pl,max}$ for different Sr_c across the range of α_0.

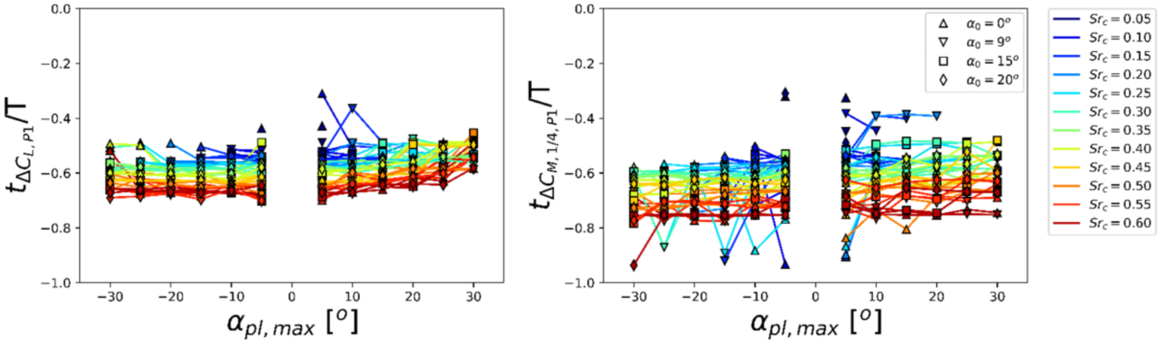

Figure 11. Normalized time of 1st peak in lift coefficient and pitching moment coefficient with $\alpha_{pl,max}$ for different Sr_c across the range of α_0.

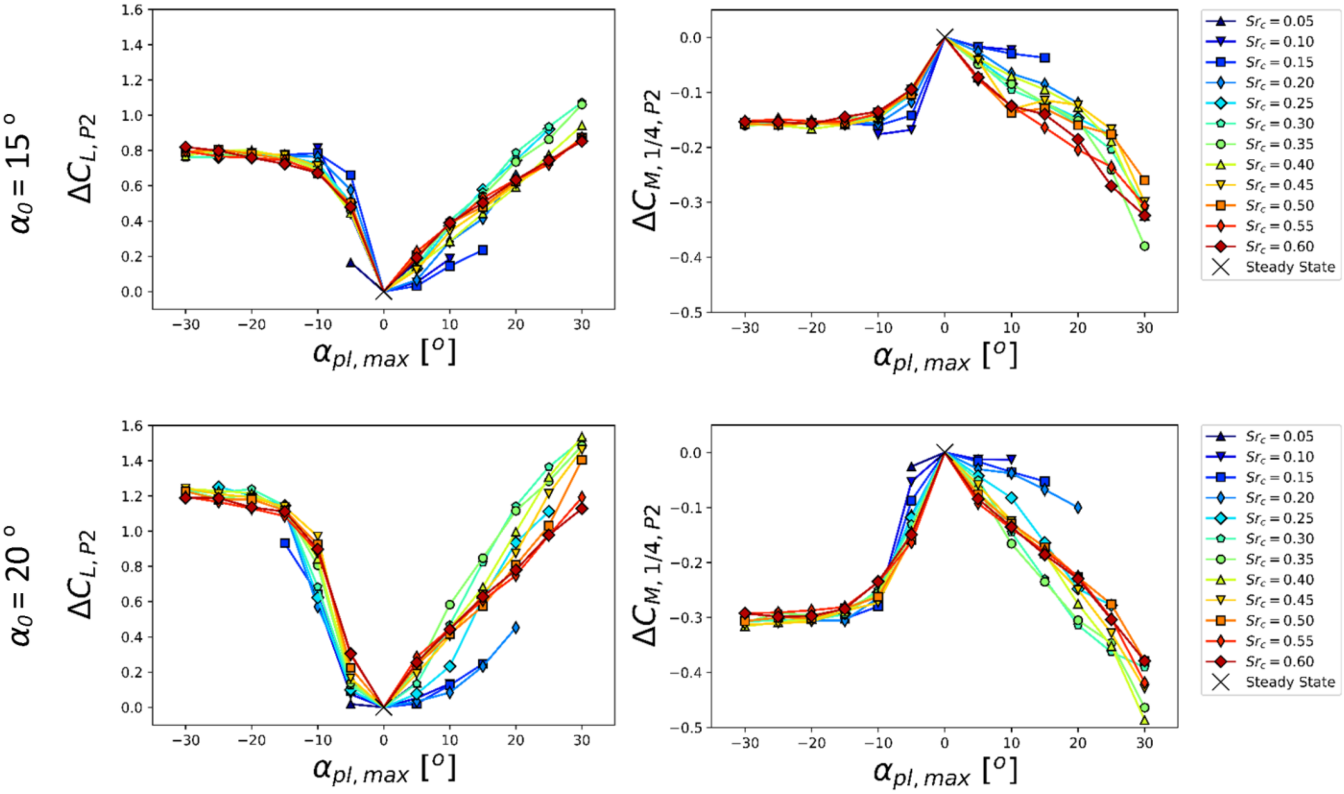

Figure 12. 2^{nd} **peak relative lift coefficient,** $\Delta C_{L,P2}$**, and pitching moment coefficient,** $\Delta C_{M,1/4,P2}$**, with** $\alpha_{pl,max}$ **for different** Sr_c **for post-stall** α_0**.**

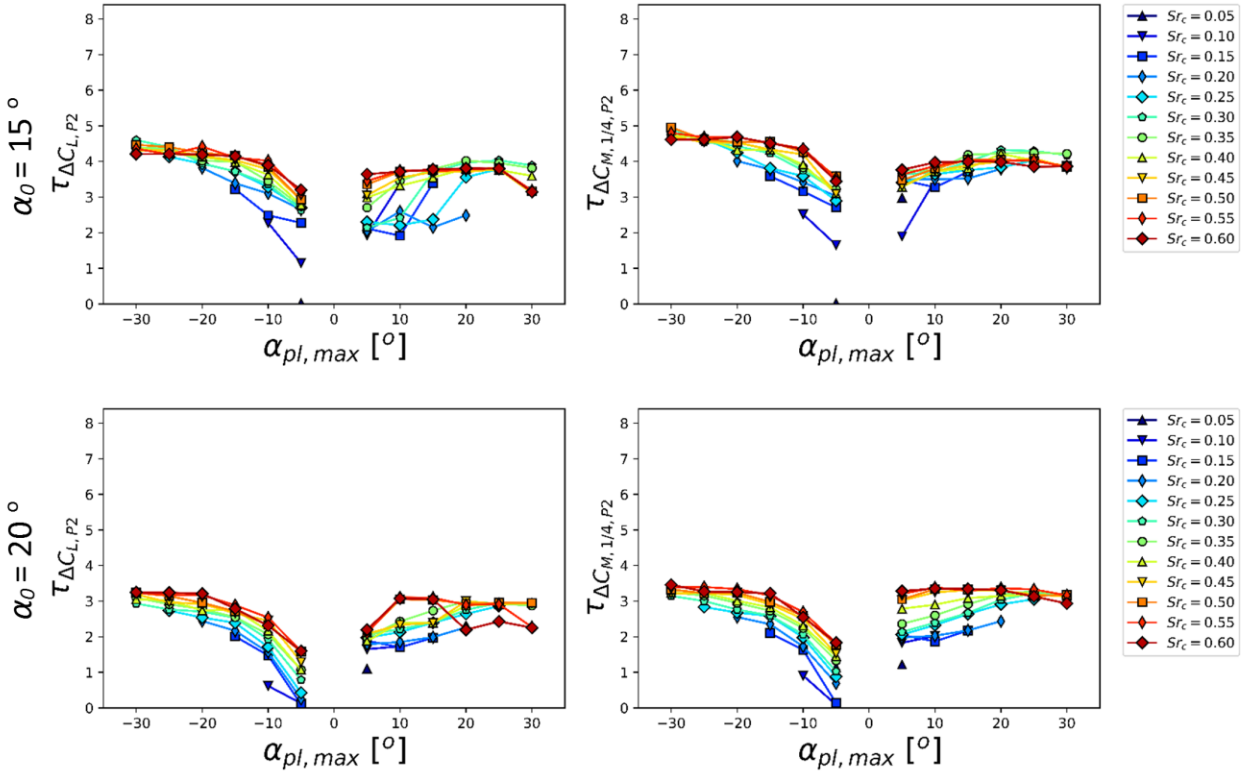

Figure 13. Convective time of 2nd peak lift coefficient and corresponding pitching moment coefficient with $\alpha_{pl,max}$ for different Sr_c across post-stall α_0.

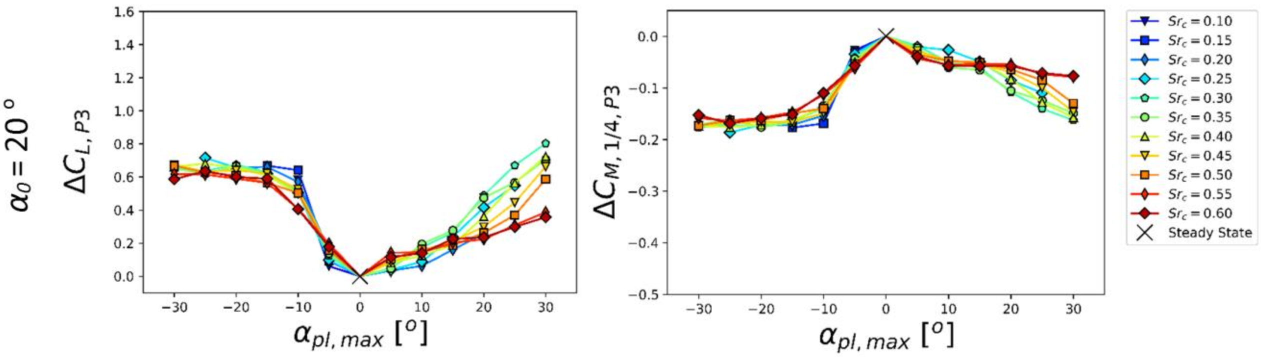

Figure 14. 3rd peak relative lift coefficient, $\Delta C_{L,P3}$, and pitching moment coefficient, $\Delta C_{M,1/4,P3}$, with $\alpha_{pl,max}$ for different Sr_c for a post-stall α_0=20°

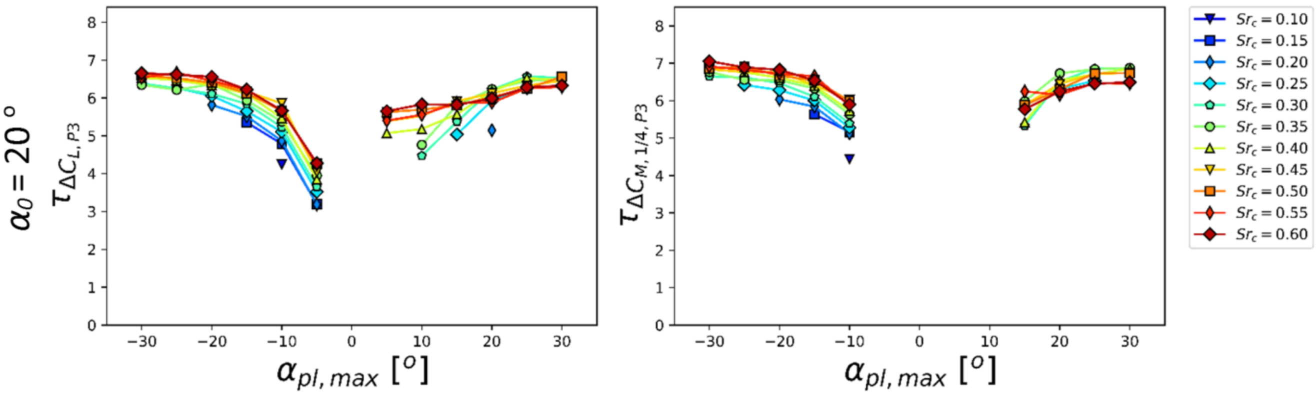

Figure 15. Convective time of 3rd peak in relative lift coefficient and corresponding pitching moment coefficient with $\alpha_{pl,max}$ for different Sr_c at a post-stall α_0=20º.